Aeroacoustic assessment of a rectilinear cascade with leading edge serrations: predictions and measurements

Martin Buszyk, Cyril Polacsek, Thomas Le Garrec, Raphaël Barrier, Vincent Clair, Edouard Salze, Christophe Bailly

AEROACOUSTIC ASSESSMENT OF A RECTILINEAR CASCADE WITH LEADING EDGE SERRATIONS: PREDICTIONS AND MEASUREMENTS

M. Buszyk[1], C. Polacsek[1], T. Le Garrec[1], R. Barrier[2], V. Clair[3], E. Salze[3], and C. Bailly[3]

[1]ONERA, DAAA, Numerical Aeroacoustic Unit, F-92322 Châtillon, France
[2]ONERA, DAAA, Helicopter, Propeller & Turbomachinery Unit, F-92190 Meudon, France
[3]Laboratoire de Mécanique des Fluides et d'Acoustique (UMR 5509), Université de Lyon, CNRS, École Centrale de Lyon, Institut National des Sciences Appliquées de Lyon, Université Claude Bernard Lyon I, 69130 Écully, France

Abstract

This study aims at evaluating previously designed leading edge serrations for the turbulence-cascade interaction noise reduction on a rectilinear cascade. Low and high-fidelity methodologies have been investigated and are compared to experimental data issued from a cascade test rig mounted in an anechoic wind tunnel. These methods include mean flow simulations for aerodynamic performance analysis, analytical models well suited to acoustic design, an Euler-based numerical method coupled with an integral method for the far-field acoustic prediction, and finally high-fidelity simulations based on the lattice Boltzmann method to take account for installation effects. The scopes and benefits of each methodology are discussed. Fast design methods and mid-fidelity numerical simulations provide satisfactory trends, but only high-fidelity simulations are able to accurately match acoustic spectra and sound power level reductions measured by microphone antenna.

Keywords: rectilinear cascade, airfoil–turbulence interaction noise, serrations, lattice Boltzmann method, computational aeroacoustics.

Introduction

Reduction of the turbulence-airfoil interaction noise represents a major challenge for the development of future quiet turbofan engines. This mechanism, expected to be a dominant contributor to turbofan noise at the certification points and more particularly at approach condition, has been widely studied in association with reduction technologies [1]. Passive treatments based on leading edge serrations have been mostly investigated

on isolated airfoils experimentally by Paruchuri *et al.* [2] among others, analytically by Ayton *et al.* [3] or numerically by Clair *et al.* [4] and Teruna *et al*. [5]. A strong noise reduction has systematically been achieved on academic geometries. For realistic turbofan configurations, only numerical predictions have been performed using Computational AeroAcoustics (CAA) [6] or lattice Boltzmann Method (LBM) [7][8], with the observation that it is much more difficult to design serrated stator vanes balancing both noise reduction and aerodynamic penalties for such cases. The rectilinear cascade configuration considered in the present study offers an intermediate step between academic and industrial cases. A similar configuration with flat plates instead of NACA airfoil cascade, has been experimented by Mazella *et al.* [9], showing a promising noise reduction with a trend similar to that obtained from a semi-empirical rule on isolated flat plates. The aim of the present work, performed in the framework of InnoSTAT project (Innovative stators) [36], is to assess the acoustic performances of serrated vanes on a rectilinear cascade configuration using most relevant prediction methodologies, previously mentioned. In particular, three approaches at different levels of fidelity are investigated: (i) the flat plate aeroacoustic response established from the Wiener-Hopf (WH) technique [3] and extended to finite span flat plates [6], (ii) hybrid Computational Fluid Dynamics (CFD) – CAA prediction including a fully three-dimensional synthetic turbulence injection and the application of the Ffowcs Williams and Hawkings (FWH) analogy [10], (iii) high fidelity simulation based on LBM [11][12]. The emphasis here is on high fidelity simulations which are shown to provide very accurate aeroacoustic predictions.

The text is structured as follows. First, the cascade test rig is introduced. The prediction approaches used in this study are then briefly presented, along with the main simplifications on geometries and the associated hypotheses required to model the actual cascade, referring to previous recent studies [10][11][12][13]. Additional details are also provided here on the LBM numerical set-up. In the third and fourth sections, aerodynamic and acoustic analyses are presented respectively. In parallel, a 1-D analytical correction model is proposed and validated to account for turbulence grid geometries. Finally, the impact of the different modeling assumptions on the noise reduction assessment, in terms of delta power level spectrum, is discussed.

1. Experimental turbulence-cascade interaction set-up including serrated vanes

1.1 Rectilinear cascade test-rig with turbulence grid

Figure 1. Picture of the subsonic and supersonic anechoic wind tunnel at LMFA.

The test campaign is conducted within the European project InnoSTAT [36] which aims at providing and evaluating breakthrough technologies to achieve low-noise OGV stages. The experiments are conduced in the subsonic anechoic wind tunnel at the fluid mechanics and acoustics laboratory (LMFA, see Figure 1). The flow is generated by a 800 kW Howden double stage centrifugal fan, delivering a mass flow rate around 20 kg/s. Air passes through a settling chamber including honeycombs and several wire meshes designed to reduce free stream turbulence. Acoustic liners on the wind tunnel walls and baffled silencers allow to reduce the noise level and to prevent contamination of acoustic measurements performed in the anechoic chamber (Figure 1). This results in an air flow with a low background noise and a residual turbulence intensity lower than 0.5%.

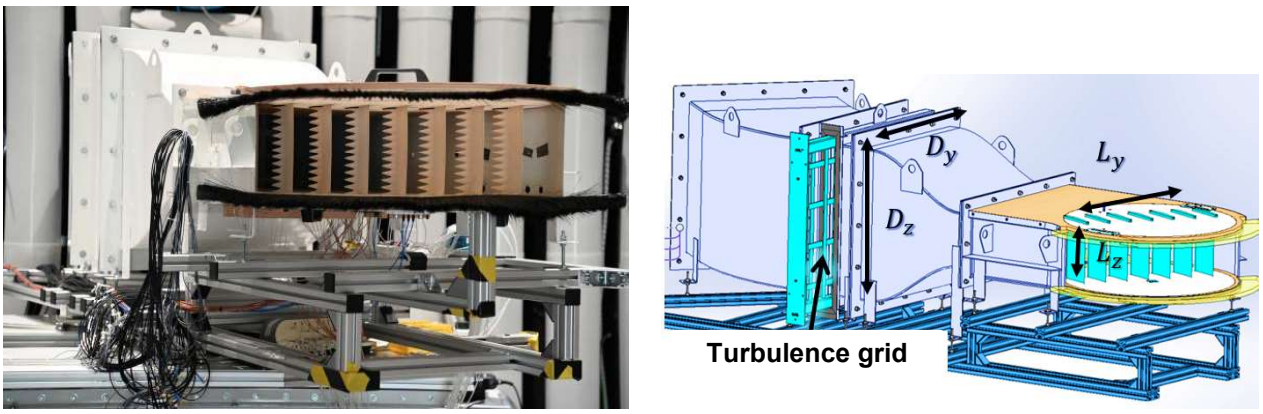

Figure 2. Picture of the cascade test rig (left). 3D geometric modeling of the bench with turbulence grid and vanes in cyan (right).

A dedicated test section depicted in Figure 2, has been designed for this experimental test campaign. It consists of a rectilinear cascade [13]. A 0.5 m long contraction adapts the test section from 0.56×0.56 m^2 to 0.56×0.2 m^2. The flow is accelerated through this nozzle in order to reach a mean value up to 180 m/s.

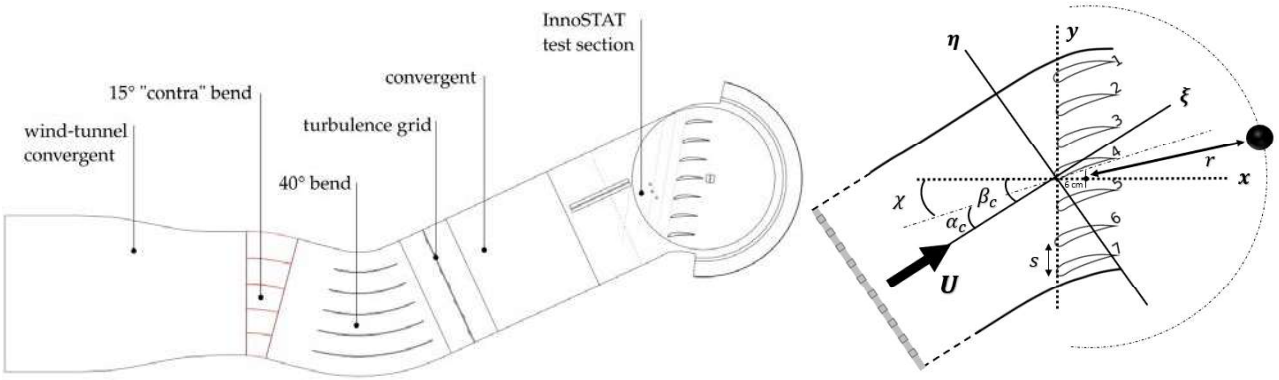

Figure 3. Schematic view at mid span cut of the test section geometry (left). Zoom on the cascade region with definition of the coordinate systems (right).

In the thinner part of the test section, seven evenly spaced NACA7310 airfoils are mounted on a rotating disk to modify the cascade angle (between the incident flow and the normal to the cascade frontline) around the nominal value β_c = 34°, see Figure 3. The stagger angle is kept at a constant value χ = 13° and the leading edge of the central vane is located at about 0.5 m downstream of the test section contraction. Vertical side plates guide the flow down to the trailing edge of the cascade, while the horizontal plates extend

downstream of the cascade as a semicircle centered on the trailing edge of the central vane. The cascade vanes are impinged by a turbulent inflow, which is generated by a turbulence grid made of rectangular rods placed in the test section just upstream of the contraction (Figure 2 and Figure 3).

	Parameter	**Value**
Airfoil	Shape Chord Span Inter-vane space s	NACA7310 12 cm 20 cm 8.5 cm
Upstream Flow	Velocity Mach Angle between cascade and flow axis β_c	45 m/s to 180 m/s M = 0.13 to M = 0.52 34° (nominal) ± $\Delta\beta_c$
Turbulence grid	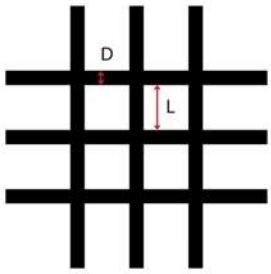	<u>Pre-test grid</u> D = 1 cm L = 4 cm <u>Tested grid</u> D = 2 cm L = 5.5 cm

Table 1. Main parameters of the test campaign.

The main parameters of the test campaign are gathered in Table 1. The grid initially proposed had a pattern is expected to generate a turbulent intensity (TI) of 4.5 % and an integral longitudinal length scale L_l of 8-9 mm, both quantities probed at 50 cm from the grid [15]. These values were adopted in the numerical simulations conducted before the tests. However, due to experimental constraints and planning requirement, a different grid was fitted to the present rig. Geometrical characteristics of both grids are compared in

Table 1. The sensitivity of aeroacoustics to the grid geometry is discussed in sections 3 and 4.

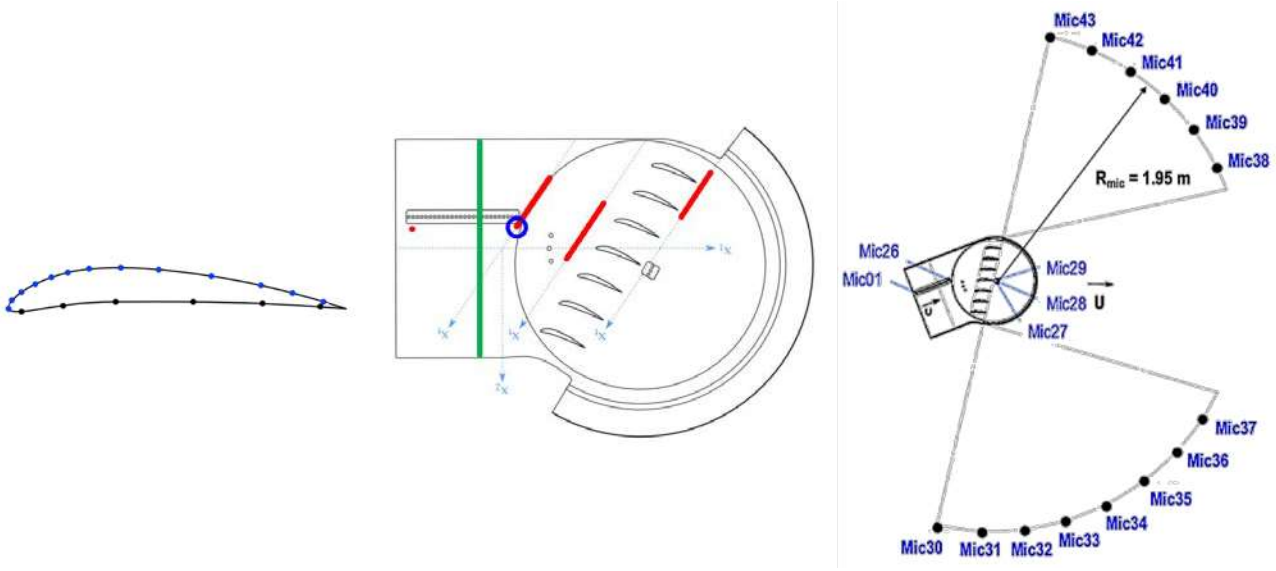

Figure 4. Pressure probes at the vane surface (left). Mid span cut of the geometry and wire probes locations (center). Far-field acoustic microphones (right).

As concerns the instrumentation illustrated in Figure 4, airfoil chordwise probes are distributed at mid-span, over the pressure and suction sides of the central middle vane (Figure 4, left), in order to measure the wall pressure coefficients. Static pressure probes are flush-mounted in the transverse direction of the test section (Figure 4, center) to check the flow homogeneity. Moreover, hot wire anemometry at midspan allows the characterization of the incoming turbulence, particularly the one-dimensional spectra at the blue circle location. Cross wire probes also measure the 2-components velocity profiles along the red lines. Finally, acoustic measurements are performed both upstream and downstream of the cascade. The positions of the 43 microphones are plotted in Figure 4, center and right. Present predictions are restricted to the far-field circular array containing 14 microphones (Figure 4, right) and centered on the trailing edge of the central vane with a radius of 1.95 m. These microphones are located in the mid-span plane, with an angular spacing of 10° from -90° to +90°. No microphone is located in the turbulent wake of the cascade between -20° and +40°.

1.2 Design of airfoils with leading edge serrations

As already discussed in [10], the leading edge serrations based on regular sinusoidal patterns were designed by applying empirical rules and backgrounds following [2] and the recent work published by Polacsek *et al*. [6], which has focused on the serration design for turbomachinery applications along with the implementation and extension of the analytical model from Ayton *et al.* [3] to finite span airfoils. The serration wavelength λ_s was set equal to twice the pre-test targeted value of the longitudinal length scale of turbulence ($\lambda_s = 4\,L_t = 2\,L_l \approx 16$ mm), and the ratio h_s/λ_s (h_s, the serration amplitude) was set equal to 1.

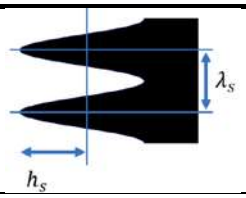	**Shape at the root**	**Shape at the peak**	**3D shape**
Design d_1 $c_{root} = c_{ref} - h_s$ $c_{peak} = c_{ref} + h_s$			
Design d_2 $c_{root} = c_{ref}$ $c_{peak} = c_{ref} + 2h_s$		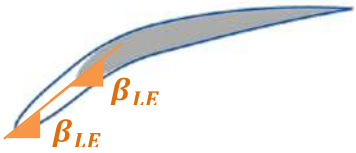	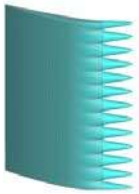

Table 2. Definitions of the ONERA designs at peak and root of the serration.

This 2D flat plate design was extended to the actual 3D airfoil by applying a suited morphing of the skeleton (with respect to thickness and camber laws) using ONERA's in-house modeler (*ersatZ)*. The serration's wavelength has been slightly adjusted to achieve an integer number of patterns along the span. A first design (d_1) was obtained by keeping the mean chord equal to the reference chord ($c_{mean} = c_{ref}$). Then, a second design (d_2), aiming to reduce the aerodynamic penalties has been proposed by imposing the reference chord at the roots, instead of sinus cancellations. The definition and geometry of

the two designs are summarized in Table 2. As demonstrated in [10], this simple increase of the mean chord ($c_{mean} = c_{ref} + h_s$) has led to a significant decrease of the pressure loss and outlet angle deviation.

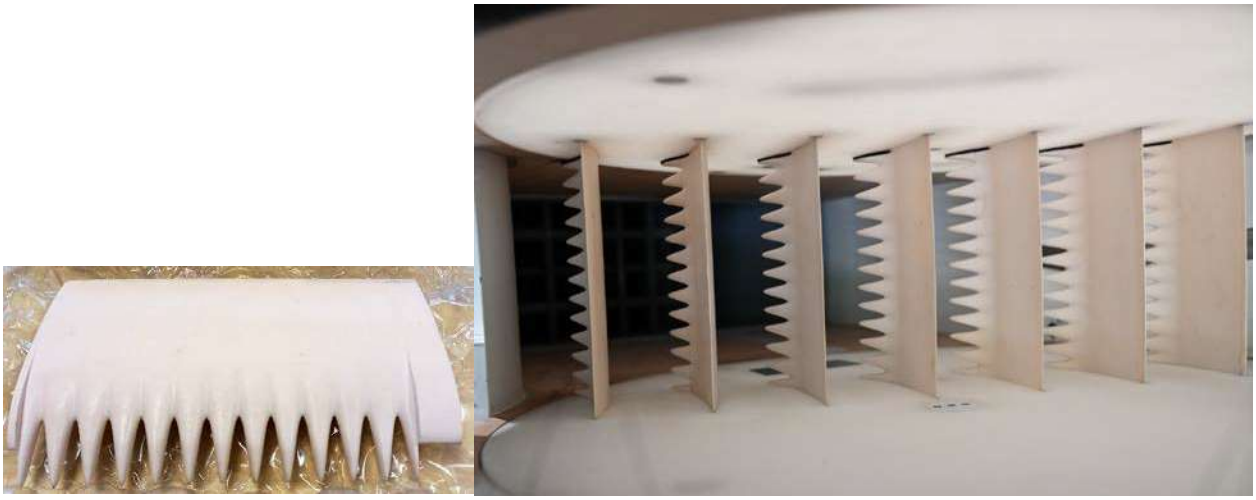

Figure 5. Pictures of ONERA serrated vanes (design d1): manufactured vane with sided-attachments (left) and 7-vanes cascade in the test rig (rear view, right).

These two treatments were manufactured using 3D printing. Pictures of the serrated vanes (design d_1) including the sided attachments for practical installation in the test section are shown in Figure 5.

2. Methods for aeroacoustic predictions applied to the cascade configuration

2.1 Analytical solution based on Wiener-Hopf formulation

The acoustic behavior of the baseline and low-noise geometries are evaluated by a state of the art analytical solution derived for a semi-infinite flat plate accounting for any piece-wise linear periodic wavy leading-edge [3]. This analytical model makes the following assumptions: a uniform convective velocity parallel to the chord, a semi-infinite plate (in the chordwise and spanwise directions), a periodically patterned leading edge. The acoustic perturbation potential satisfies the Helmholtz convective equation, and the incoming gust is only represented by a single vector component normal to the chord with a 2D planar wavenumber spectrum from a homogenous isotropic turbulence (HIT). The

final asymptotic solution of the acoustic pressure in the far-field is derived by solving the convective Helmholtz equations by means of change of variables and the Wiener-Hopf (WH) technique. For solving the complex integral obtained with the Wiener-Hopf technique, the steepest descent approximation is used.

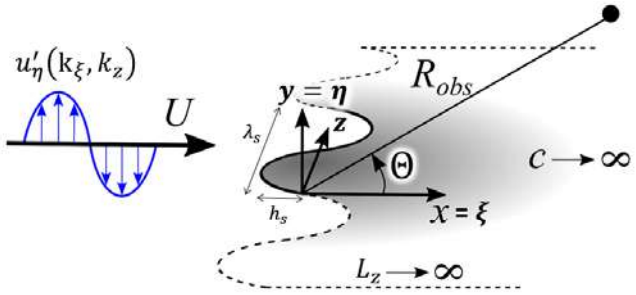

Figure 6. Sketch of the configuration used by the analytical model.

The present problem solved by the analytical model is sketched in Figure 6, involving a flat plate with here a sinusoidal leading edge shape of amplitude h_s and length λ_s. It can be noted that an asymptotic geometrical correction allowing to deal with finite span airfoils (without using any calibration from a reference solution) has been proposed with validations and applications being addressed in [6][34].

2.2 Computational aeroacoustic with an incoming synthetic turbulence field

Mid-fidelity predictions can be obtained from a first numerical approach involving CAA with a synthetic turbulence injection. The actual 3-D geometry of the airfoils (with/without serrations) is now fully accounted for, but we are assuming an infinite rectilinear cascade (several vane channels with periodic boundary conditions) and a prescribed turbulent inflow derived from a HIT model (as in the previous analytical solution from 2.1). The CAA simulations are achieved using an ONERA's parallelized time-domain code *sAbrinA*. It computes noise generation and propagation on multi-block meshes which are curvilinear and structured. It can solve both the non-linearized and linearized Euler equations written in a perturbation and conservative form, which are detailed in [17] and reminded in [18] (Appendix B). Here, the linearized Euler equations have been solved since the non-

linearity has an effect on the acoustic only for gusts of high amplitude i.e. around 10% of the mean flow, as discussed in [18]. The unsteady flow field is classically split into two parts, namely the mean flow, which has to be provided as an input, and the fluctuating part, which temporal evolution is computed by the code. Regarding numerical schemes, *sAbrinA* uses a standard 6th order finite difference scheme for the spatial derivatives and a third-order multistage explicit Runge–Kutta scheme for the time integration. Specific treatments and boundary conditions (BC) are implemented, such as a 10th order explicit filter in order to remove high frequency oscillations and Tam and Dong boundary conditions [19], which are used to allow both the exit and entrance of the prescribed fluctuations in the domain without generating neither spurious noise sources nor numerical reflections. The turbulent inflow is generated through a stochastic process, based on a Fourier-mode decomposition and adopting Liepmann model for isotropic turbulence, and injected at the entrance of the CAA domain.

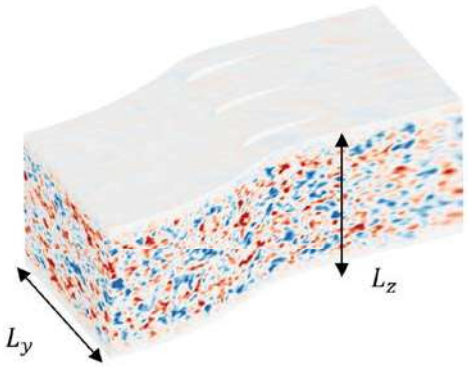

Figure 7. Turbulent-like u'_y snapshots (levels between $\pm 10\ m \cdot s^{-1}$) for $(k_\xi,\ k_\eta, k_z)$ turbulence structure (taken from [10]).

A 3D solenoidal turbulence field generation procedure accounting for periodic and wall boundary conditions has been implemented and validated on a 3 vanes passages computation in [10] with periodic boundary conditions, and illustrated in Figure 7. As shown in [10], the 3 vanes represent a good compromise in terms of noise prediction and CPU cost. Since the near-field propagation domain is limited, the far-field acoustic solution is obtained by radiating the pressure sources at the vane skin using a Ffowcs Williams-

Hawkings (FWH) analogy with a free-field Green function. This step is practically achieved using the in-house code (*MIA)*, solving the loading noise term of the FWH integral, written in the frequency domain following [18][20].

2.3 High fidelity lattice Boltzmann approach

High-fidelity numerical simulations based on the lattice Boltzmann Method (LBM) aim to provide the most accurate aeroacoustic assessment, capturing the actual turbulent sources and sound radiation by considering the full test section in the computational domain including the grid which generates the incoming turbulence resolved in the simulation. Contrary to traditional CFD solvers relying on the Navier-Stokes (NS) equations, the LBM is a mesoscopic approach originating from the kinetic theory of gases. The fluid is described by probability distribution functions of fluid particles. In practice, the fluid velocities are discretized on a lattice, which acts as the mesh of the simulation. On this lattice, the evolution of the distribution function can be governed by a two-step algorithm often called "stream and collide". Collisions take place locally and the streaming operation is performed following the octree lattice and is exact thanks to the Courant-Friedrichs-Lewy (CFL) equal to 1, which makes this step non-dissipative and its numerical implementation quite simple and cost effective since coarser mesh cells have a smaller time step. As a consequence, the solver efficiency and the very low numerical dissipation suitable for aeroacoustic simulations. Additionally, immersed boundary conditions handle geometries, around which the fluid boundary layer is resolved thanks to an advanced wall log-law taking into account an adverse pressure gradient and curvature effects [38][39]. In the present work, LBM simulations are carried out with the *ProLB v2.6.3* solver [22]. In this study, the weakly compressible version of the solver has been used. For quasi-incompressible flows, the discrete distribution function involves nineteen velocities, also called D3Q19 allowing the computation of the athermal formulation of the NS equations [23]. In *ProLB*, an advanced collision operator, the hybrid recursive regularized (HRR)

operator is implemented, enhancing the stability of the scheme and reducing the spurious noise at mesh refinement transition along with high order correction terms to remove $o(M^2)$ errors [24][25], leading to a more robust code below M=0.7 [26][27]. As for the advection of the variables across grid refinements, the Direct Coupling (DC) cell-vertex algorithm is used [25][28]. It helps reducing spurious noise source generation at mesh transitions. Similarly to traditional CFD solvers, a Large Eddy Simulation turbulence model controls the unresolved small-size turbulent dynamics. In ProLB, the Shear-Improved Smagorinsky Model (SISM) [29] is employed as a subgrid-scale viscosity to model unresolved eddies.

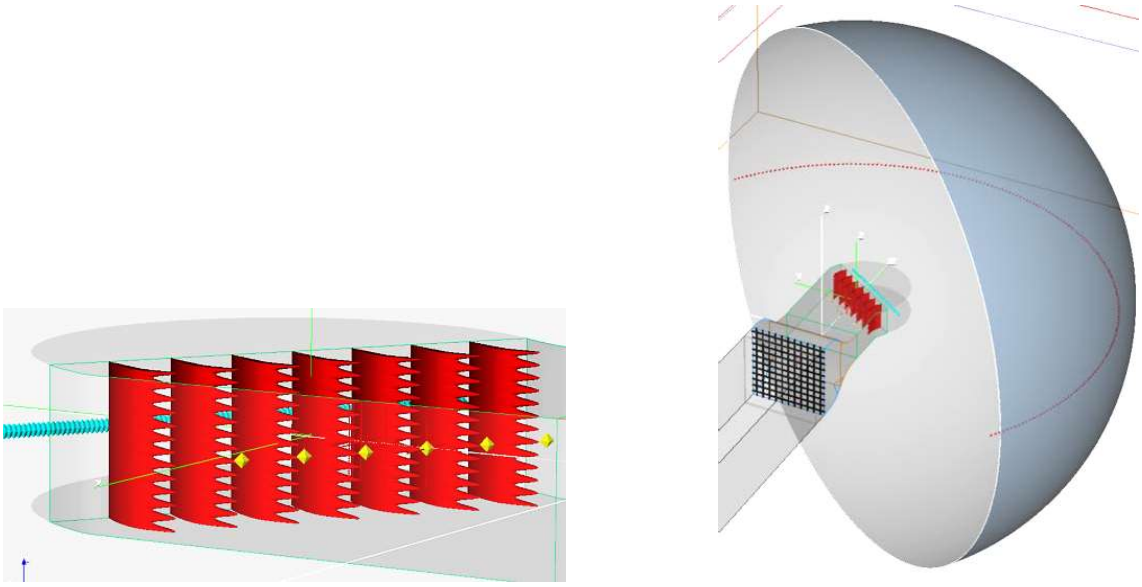

Figure 8. View of the cascade geometry with serrations (left). View of the test rig geometry (right).

The key idea behind high-fidelity simulations based on the LBM is to easily take into account the full test section in the numerical domain. In particular, the present set-up takes into account the seven vanes cascade, the nozzle, as well as the horizontal and side plates, and the turbulence grid, as illustrated in Figure 8. Furthermore, the low dissipative behavior of the LBM previously reminded enables direct far-field acoustic predictions with probes located in the numerical domain at the same position that the experimental semi-circular microphone array. However, indirect noise calculations can also be performed using the FWH approach as for the CAA method.

The lattice Boltzmann simulation set-up introduced below has been obtained after successive improvements summarized in [10][11]. It represents the finest grid which has been used during the numerical process.

Parameter	Value
$\Delta x_{min} = \Delta y_{min} = \Delta z_{min}$	0.2 mm
Reference c_0	343 m/s
Δt	$3,36 \cdot 10^{-7}$
Number of Iterations (It)	$1,2 \cdot 10^{6}$
Simulated time (T)	0.404 s
SISM cut-off frequency	15 kHz
Inflow velocity condition (applied upstream of the grid)	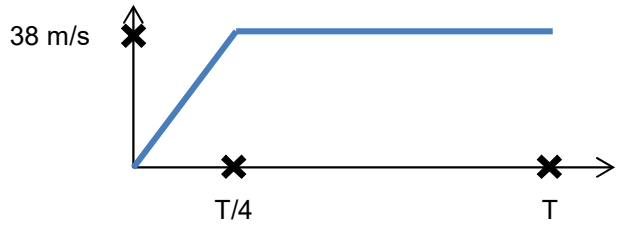

Table 3. Numerical parameters of the simulations. SISM refers to the Shear-Improved Smagorinsky Model. Inflow condition denotes the velocity condition (in m/s) imposed at the entrance of the test section.

The key parameters of the simulation are gathered in Table 3. It should be noted that the operating inflow condition is driven by a velocity injection law in a plane upstream of the turbulence grid. For the mesh, the finest cell size of 0.2 mm is located in the refinement region directly around the vanes.

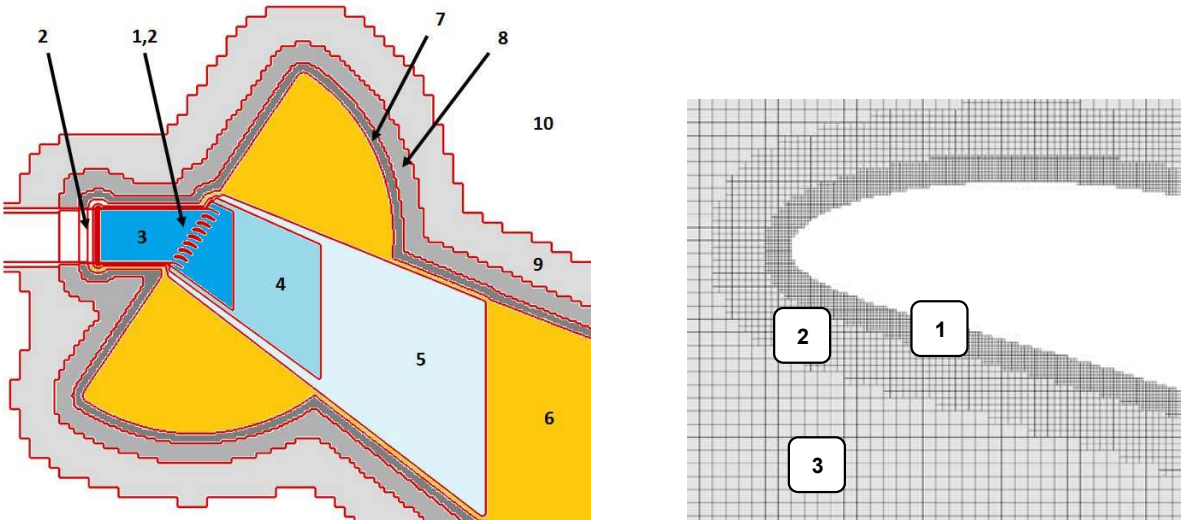

Figure 9. Mesh refinement levels in the plane z = 0 (left). Octree mesh for the "fine mesh" configuration around a NACA airfoil LE (right). With the number denoting the mesh level in the aera from Table 4.

In Figure 9 (right), a cut of the octree mesh close to the NACA leading edge is presented, showing two successive layers of mesh with 8 points each (above the minimum recommended value of 6), with a chordwise resolution of nearly 600 points at the finest level. The separations between the following consecutive grid refinement levels are plotted in Figure 9 (left). The zone index is indicating the level of grid refinement. Inside the test section (zone 3), a 14 points per wavelength discretization is ensured for the capture of turbulent structures up to 10 kHz. As for the acoustic area (zone 6) the minimal recommended value of 8 point per wavelength is satisfied up to about 6.5 kHz. The choice to not refine the acoustic area further has been made to limit the total number of points which would otherwise dramatically increase. Finally, mesh transitions in the wake are spaced and aligned with the mesh in order to enhance the DC (Direct Coupling) algorithm efficiency at spurious noise reduction.

Zone n°	1	2	3	4	5	6	7
Mesh size (m)	0.2	0.4	0.8	1.6	3.2	6.4	12.8
Points in zone (%)	≈ 6	≈ 3	≈ 34	≈ 14	≈ 11	≈ 29	≈ 1
Eqv. Fine points in zone (%)	≈ 31	≈ 8	≈ 44	≈ 9	≈ 4	≈ 5	≈ 0

Table 4. Mesh characteristics at each discretization level.

Mesh size, and relative contribution to overall number of points are summarized in Table 4. Equivalent fine points (Neqv) denotes the number of points (N) weighted by its computational cost (since in LBM, coarser grids have a larger time step due a CFL=1 constraint everywhere) following (with $\mathrm{N_i}$ the number of points and $\widetilde{N_\mathrm{i}}$ the number of equivalent points in a zone i):

$$\widetilde{N_\mathrm{i}} = \mathrm{N_i}\left(\frac{1}{\mathrm{i}}\right)^{\frac{1}{2}} (0)$$

For instance, the discretization inside the test section (for advection of the turbulence structures) is the main contributor to both the CPU cost and RAM usage. The second major component of the CPU cost is the zone directly surrounding the vanes.

Geometry / Parameter	Baseline	Design d_1	Design d_2
CPU cores	≈ 4000	≈ 4000	≈ 8000
Solver restitution time (days)	≈ 3.5	≈ 3.5	≈ 2
CPU core time (hours)	≈ 300k	≈ 320k	≈ 400k

Table 5. HPC characteristics of LBM simulations on ONERA's supercomputer Sator.

The main HPC features of these simulations are presented in Table 5. In particular, these LBM simulations provided an opportunity to test *ProLB* scalability up to 8000 cores, with an acceleration factor of 1.6 in comparison with the 4000 core case.

3. Aerodynamic analysis

3.1 Mean flow assessment

For the convergence towards the experimental operating point, the target inflow velocity regime has been measured at a distance of one chord upstream of the vane cascade at the center of the test section. By considering a time ramp on the inflow velocity condition (see Table 3), the transient time has been reduced along with an improved stability of the computation. Without this velocity ramp, an overshoot of the velocity magnitude has been observed which could lead to a crash of the simulation.

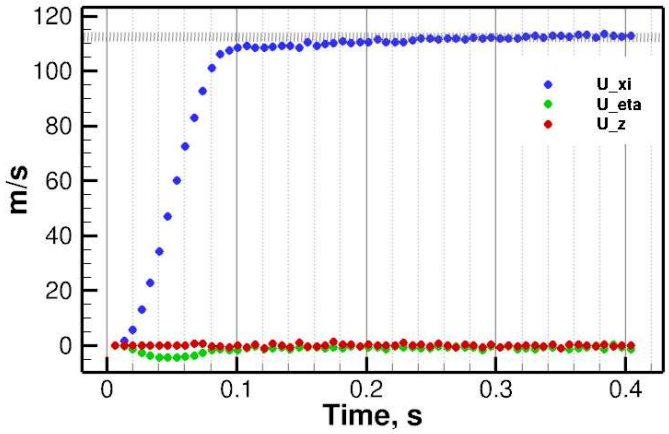

Figure 10 Mean flow convergence along each space direction.

In Figure 10, a good convergence of the mean flow properties is obtained after a transient time of approximately 0.2 s. The wall pressure coefficient Cp is evaluated on the reference vane at mid-span according to:

$$\mathrm{Cp} = \frac{p - p_{ref}}{\frac{1}{2}\rho_{ref} U_{ref}^2} \quad (1)$$

where ρ_{ref}, U_{ref} denote the mean values measured half a chord upstream of the airfoil. The wall pressure coefficient was measured on the vane centered in the test section at a flow velocity of 117 m/s (M=0.34), and compared to RANS and LBM predictions.

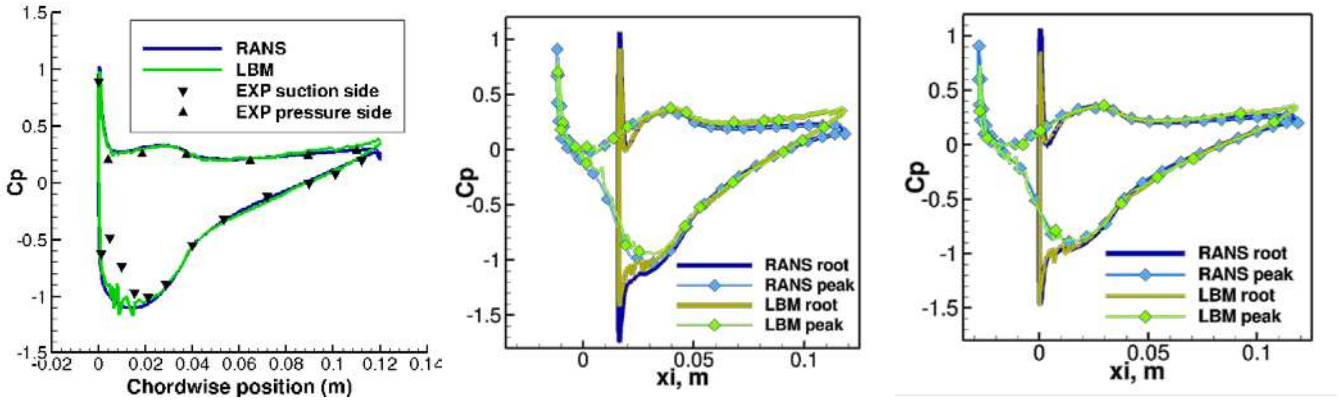

Figure 11. Cp distribution on the central vane at mid-span for the baseline configuration at M=0.34 (left). Cp profile of the central vane at mid-span for the serrated designs d_1 (center) and d_2 (right).

A fairly nice agreement is observed between the three approaches in Figure 11, despite small oscillations on the suction side visible on the LBM results. Indeed, in this region, large curvature induces steep geometrical variations of the intersection between the immersed boundary conditions and the octree mesh, which may produce some oscillations in the boundary solution. The Cp profiles for the serrated geometries d_1 and d_2 (see Figure 11, center and right) are also extracted at the peak and root locations around mid-span. Again, a good agreement has been found with the RANS solutions, even if a larger deviation can be observed near the trailing edge in particular for the d_1 configuration compared to the baseline and d_2 cases.

3.2 Turbulent flow characterization

The interaction noise radiated from the cascade is directly related to the upstream turbulent flow generated by the turbulence grid. Thus, a reliable capture of the main turbulence characteristics is of interest for noise predictions on the baseline and serrated designs d_1 and d_2 discussed in [10].

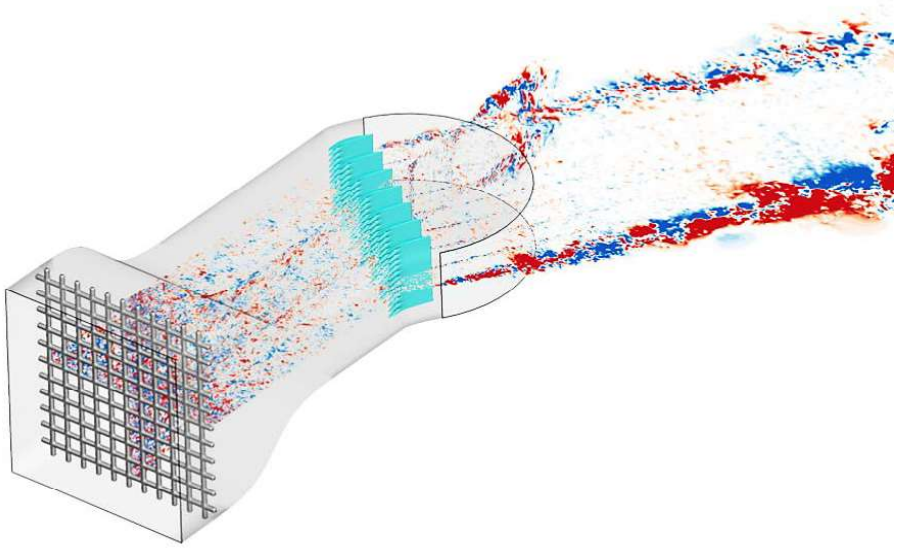

Figure 12 Snapshot of the fluctuating velocity field at mid-planes of the section.

A color map of instantaneous u'_η fluctuating velocity field in the mid-planes of the test section is depicted in Figure 12. The turbulent longitudinal length scale L_l is computed from the turbulence velocity spectrum as follows:

$$L_l = \lim_{f \to 0} \left(\frac{S_{u'_\xi u'_\xi}(f) U}{4 \langle u'^2_\xi \rangle} \right) \quad (2)$$

where $S_{u'_\xi u'_\xi}(f)$ denotes the one-sided Power Spectrum Density (PSD) of the streamwise velocity component. This definition relying on the frequency domain can be more relevant than its temporal counterpart, when the very low frequency response is not perfectly converged, as it can be easily discarded in Fourier space. Regarding the turbulence intensity, a directional definition is considered to evaluate the isotropy hypothesis. For the streamwise direction, one considers:

$$\mathrm{TI}_\xi = \frac{\sqrt{\langle u'^2_\xi \rangle}}{U} = \frac{\sqrt{\int_0^\infty S_{u'_\xi u'_\xi}(f) \mathrm{d}f}}{U} \quad (3)$$

and the mean turbulence intensity denoted TI, with η the upwash direction and z the spanwise one, is then classically obtained as:

$$\mathrm{TI} = \sqrt{\frac{1}{3}\left(\mathrm{TI}_{\xi}^{2} + \mathrm{TI}_{\eta}^{2} + \mathrm{TI}_{z}^{2}\right)} \quad (4)$$

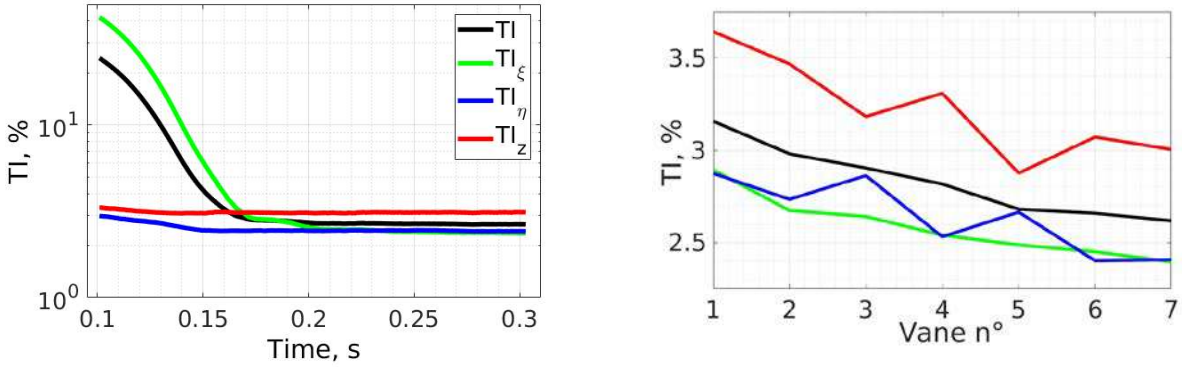

Figure 13. Temporal evolution of turbulence intensities using a moving average over 0.2 s (left). Converged turbulence intensities in front of each NACA airfoil (right).

Convergence is achieved after a transient time of approximately 0.2 s, as illustrated in Figure 13 (left) for the fluctuating velocities expressed in terms of directional turbulence intensity. It is interesting to note the amplification of the z-component, which might be due to the fact that the contraction of the test section is very strong (ratio 2.8) and only along this z-direction. As a result, the turbulence field is not perfectly isotropic. In Figure 13 (right), the variation of turbulent intensities is plotted along the cascade direction. It indicates that the blades are not uniformly impacted by the turbulent inflow, which is therefore not perfectly homogeneous. Turbulent length scales can be also recovered from spatial correlations by applying the classical expressions from literature ([35] or Eq. (III.25) and Eq. (III.26) in [34])). To that end, crossed lines of probes are considered, located half a chord upstream of the central vane.

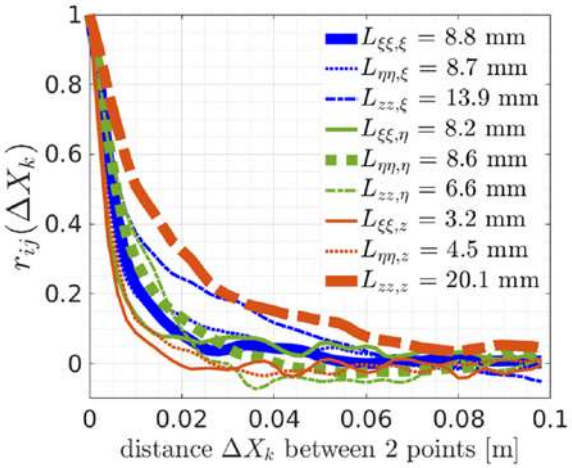

Figure 14. Turbulent length scales $L_{ij,k}$ evaluated at a half chord upstream of the central vane.

The oscillations noticed in Figure 14 reveal that the turbulent length scale post-processing from spatial correlations remains quite challenging. However, several key aspects can be deduced from Figure 14. A strong anisotropy of turbulence is present which is not consistent with analytical models and synthetic turbulence assumptions. Nevertheless, it is interesting to note that $L_{\eta\eta,z}$ which corresponds to the spanwise correlation length of the upwash velocity component (theoretically equal to half the longitudinal integral length scale L_l) is close to the serration design parameter L_t = 4 mm. Indeed, serrations wavelength $\lambda_s = 4L_t$ has been chosen to maximize the noise reduction according to semi-empirical models [2]. In the following, the focus is put on turbulence properties analysis based on velocity spectra, which seems more relevant and accurate in cases where mesh discretization is not fine enough to estimate spatial correlations.

3.3 Turbulent spectra and 1D correction to account for turbulence grid parameters

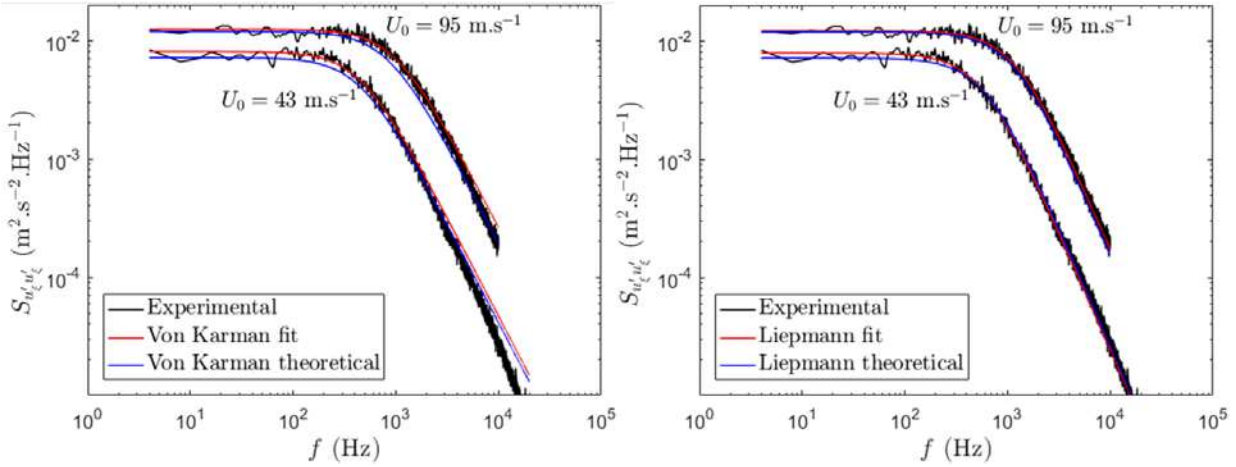

Figure 15. Turbulent velocity spectra of the axial velocity component obtained during the experimental test campaign for two incident flow regimes.

The single component turbulent axial velocity spectra obtained from a single hot-wire probe at the location circled in blue in Figure 4 are presented in Figure 15 for two incident flow velocities, U_ξ = 45 m/s and 95 m/s (the highest reachable speed for a reliable use of hot-wire data without vibration issues). In addition to genuine turbulence properties calculation, a solution relying on a least square fitting method from the turbulence spectrum has been applied. The latter is plotted in Figure 15 (in red).

	U_ξ = 43 m/s		**U_ξ = 95 m/s**	
	TI_ξ (%)	L_l (mm)	TI_ξ (%)	L_l (mm)
Theoretical (Eq. (2) and Eq. (3))	6.1	11.2	4.9	13.3
Liepmann least square fit	6.5	11.2	5.0	12.6
von Karman least square fit	6.5	11.2	5.4	11.4

Table 6. Turbulent intensity and length scale deduced from measured velocity spectra.

The estimated values of TI and L_l are provided in Table 6 for the two incident flow speeds considered. Slight variations are observed between the two incident flow velocities. Note that for U_ξ = 95 m/s, the experimental spectrum was only used up to 10 kHz because of vibration issues. The reported values of TI_ξ and L_l are deduced from expressions (2) and

(3). They can also be determined by considering the least square fits of the measured one-dimensional spectra

$$S_{u'_\xi u'_\xi}(f) = \varphi^{1D}_{\xi\xi}\left(k_\xi = \frac{2\pi f}{U}\right) \times 4\pi/U$$

with $\varphi^{1D}_{\xi\xi}$ provided by Liepmann's model [34], and consistent estimates are found. Liepmann's model here provides a very good fit to the measured data, with a decay slope in better agreement than von Karman's model. A similar work can be performed from the LBM results, where signals are extracted at the same location than in the experimental set-up, around 20 cm in front of the vane cascade.

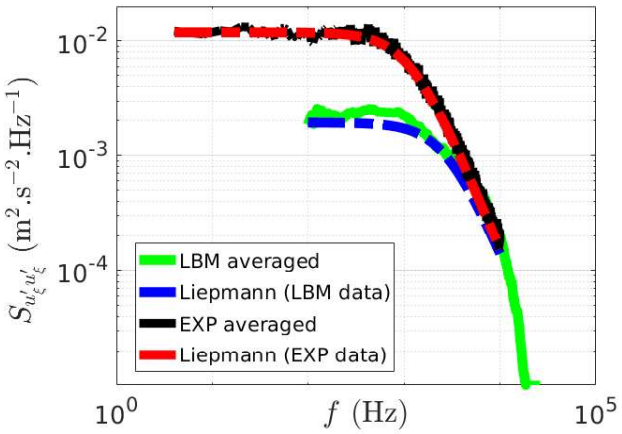

Figure 16. Turbulent velocity spectra of the axial velocity component obtained from LBM and comparisons with experiments.

In order to discard the non-relevant part of the spectra in the low frequency range, polluted by statistical errors due to a shorter time acquisition in numerical simulations, the post-processing frequency range is restricted to the band [100 Hz - 10 kHz] as illustrated in Figure 16. As a reminder, the LBM results are acquired on 0.2 s contrary to experimental values acquired during 60 s, which explains the higher convergence and smooth shape in the low frequency range, up to 10 Hz, observed in Figure 15. The respective values for TI and L_l approximately equal to 2.8% and 7 mm are obtained for both theoretical and least square methods. There is a clear gap with experimental values from Table 6. Indeed, it must be emphasized that LBM simulations have been carried out considering the a priori grid geometry with square bars of D=1 cm side and a pattern of

L=4 cm whereas an actual grid with 2 cm side bars and 5.5 cm pattern has been used in the experimental test campaign carried out after the simulations (Table 1). A correction based on the one-dimensional energy spectrum has then been proposed to be able to pass from grid to another and thus compare the numerical and experimental results. Setting $U = U_\xi$ as the mean velocity upstream of the cascade, the following correction is applied where $\varphi_{\xi\xi}^{1D}$ the one-dimensional Liepmann spectrum:

$$S_{u'_\xi u'_\xi}{}^{\mathrm{LBM,\ corr}}(f) = S_{u'_\xi u'_\xi}{}^{\mathrm{LBM}}(f)\frac{\varphi_{\xi\xi}^{1D}\left(f, U^{\mathrm{exp}}, \mathrm{TI}_\xi{}^{\mathrm{exp}}, L_l{}^{\mathrm{exp}}\right)}{\varphi_{\xi\xi}^{1D}\left(f, U^{\mathrm{LBM}}, \mathrm{TI}_\xi{}^{\mathrm{LBM}}, L_l{}^{\mathrm{LBM}}\right)}$$

$$= S_{u'_\xi u'_\xi}{}^{\mathrm{LBM}}(f)\left(\frac{\mathrm{TI}_\xi{}^{\mathrm{exp}}U^{\mathrm{exp}}}{\mathrm{TI}_\xi{}^{\mathrm{LBM}}U^{\mathrm{LBM}}}\right)^2\left(\frac{L_l{}^{\mathrm{exp}}}{L_l{}^{\mathrm{LBM}}}\right)\left(\frac{1+\left(L_l{}^{\mathrm{LBM}}\frac{2\pi f}{U^{\mathrm{LBM}}}\right)^2}{1+\left(L_l{}^{\mathrm{exp}}\frac{2\pi f}{U^{\mathrm{exp}}}\right)^2}\right) \quad (5)$$

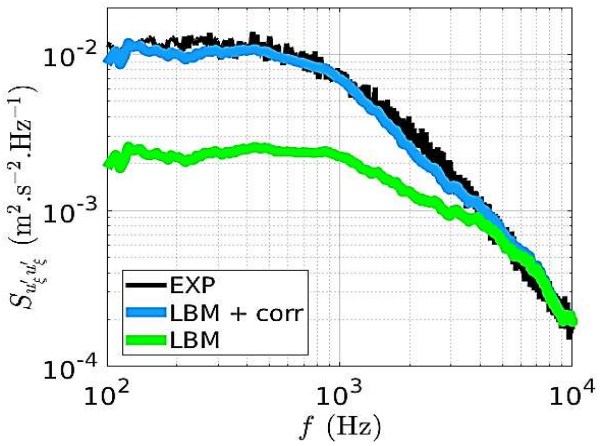

Figure 17 : Turbulent velocity spectra of the axial velocity component obtained from experimental data and LBM simulations with and without correction.

Thus, with this theoretical-based calibration, a value of TI ≈ 4.6 % and L_l ≈ 12.6 mm is now achieved with the corrected LBM spectrum, values very close to those from Table 6, giving rise to a matching between corrected LBM and experimental spectra pointed out in Figure 17. This correction is also applied in the next section to far-field acoustic spectra obtained from LBM simulations, since the radiated sound spectrum is linearly depending

on the inflow turbulence spectrum under certain hypothesis [34].

Following on from a previous collaborative study [13], complementary simulations have been carried out after the test campaign with the up-to-date grid. Turbulence and acoustic spectra provided in Appendix A (the results are not published) are in a very close agreement with the measurements, which reinforces the proposed rule (5).

4. Aeroacoustic analysis

4.1 Sound power levels and directivities

Aeroacoustic analyzes are mainly based on LBM and CAA predictions. The pressure fluctuations extracted on the vane skin issued from both methods are discussed first.

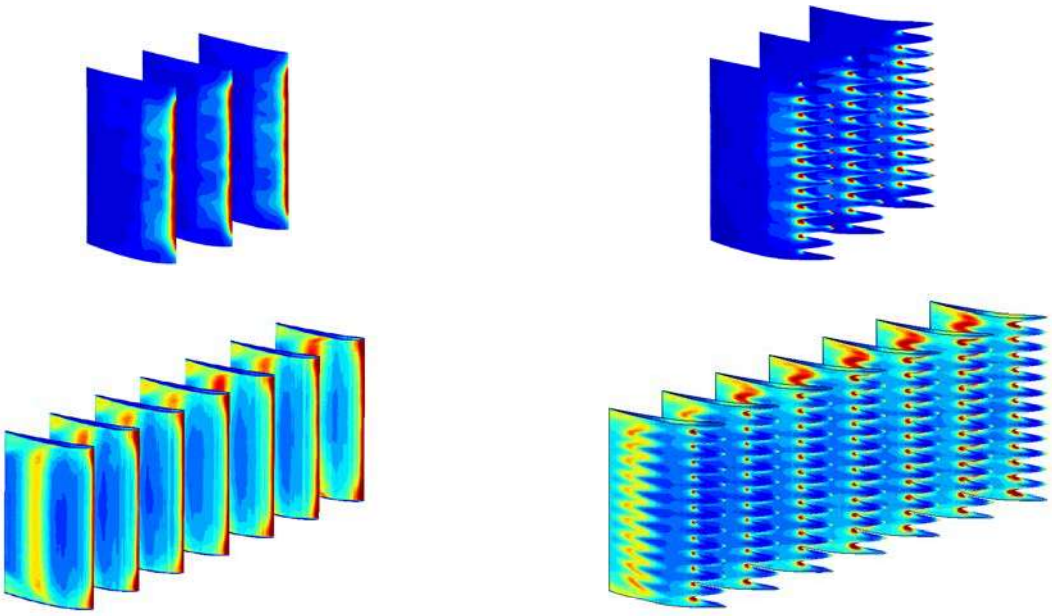

Figure 18. p'_{RMS} color maps on the vane skin (levels between 0 and 500 Pa). Baseline (left) and low-noise d_1 (right) geometries. Top: CAA. Bottom: LBM.

Figure 18 illustrates the fluctuating pressure field p'_{RMS} on the baseline and low-noise d_1 geometries. It indicates that the blades are not uniformly impacted by the turbulent inflow in LBM, which is indeed not perfectly homogeneous contrary to CAA. Two areas of high pressure values can be distinguished: the leading-edge associated with the tubulence-airfoil interaction noise and a band of fluctuating pressure at mid-chord which may be

related to local unsteady flow detachments associated with viscous effects. In Figure 18 (top right), pressure sources are clearly located at the roots of the serrations as expected from the literature and most likely giving rise to radiated sound field reduction [30][31]. Since the CAA simulates an inviscid Eulerian flow, there is no mid-chord high amplitude visible sources in Figure 18 (bottom) associated with viscous phenomena. Such additional sources (captured by LBM), quite significant in the presence of serrations (Figure 18, bottom right), might mitigate the contribution from attenuated leading edge sources. Two diffferent approaches to assess the radiated sound farfield are investigated. (1) Using a FWH analogy in the frequency domain applied to the Fourier-transformed wall pressure fluctuations for both CAA and LBM. (2) Using the direct acoustic field predicted and propagated by the LBM (referred as direct approach) from probes in the numerical domain located at the exact location of the experimental microphone array (see Figure 4). As a reminder, the probes are located in a zone where the cell size is 6.4 mm allowing acoustic waves propagation with limited dissipation up to 6.5 kHz, in order to propagate the acoustic waves.

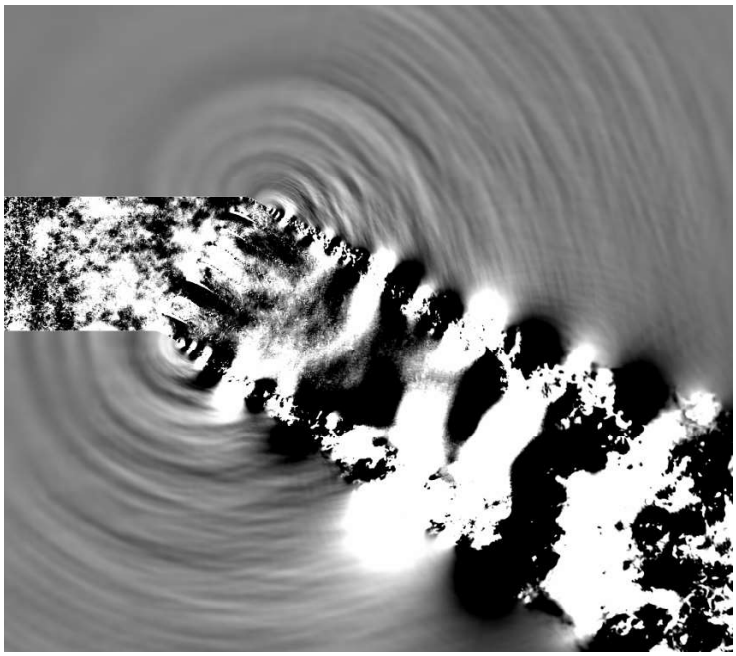

Figure 19. Visualization of the fluctuating pressure (p', levels between ±20 Pa) at mid-span in the simulation domain (M = 0.34).

A snapshot of the fluctuating pressure in the mid-span plane is provided in Figure 19.

Acoustic waves emitted from the cascade can be observed in the domain, outside of the turbulent wake. Figure 19 does not show any spurious noise source, in particular at refinement mesh transitions crossed by the turbulent wake. Moreover, shear boundary layers at the side plates are also reproduced.

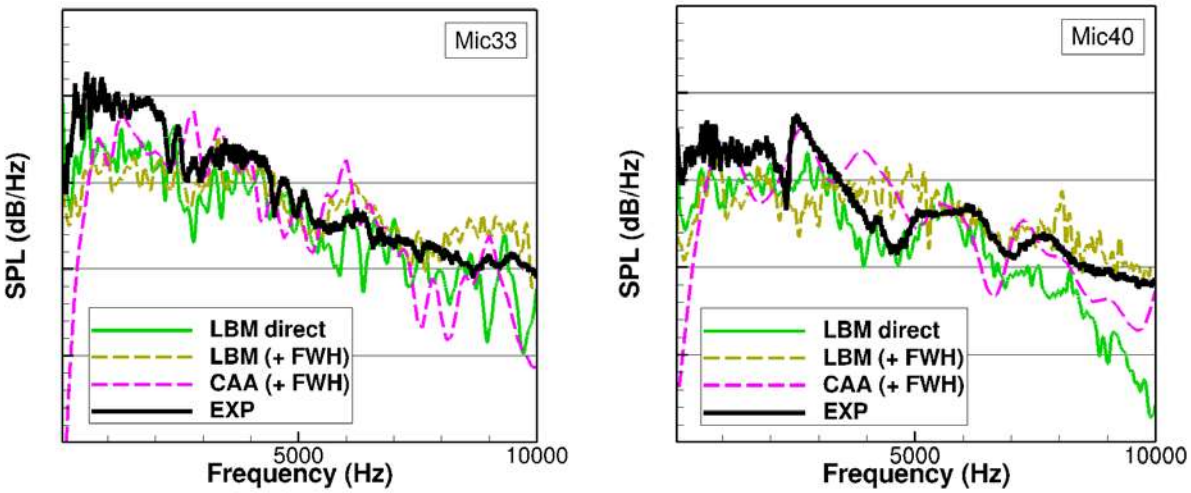

Figure 20. SPL comparisons on baseline case: numerical simulations vs. experiment at Mach 0.34 for mic. 33 (left) and mic. 40 (right). A moving averaged has been applied to smooth the spectra. Linear x-scale and 10 dB step between major y-ticks ticks (corresponding to the grid lines).

Power Spectral Densities (PSD) of the acoustic pressure expressed as Sound Pressure Level (SPL, in dB/Hz) obtained from LBM and CAA at two microphones (Mics. 33 and 40) are compared to experiment in Figure 20. Although the overall agreement seems satisfactory using a linear frequency scale, it can be pointed out that sawtooth variations sometimes visible on the experimental spectra are better captured by the LBM direct calculation, despite the numerical dissipation effects of the mesh beyond 6.5 kHz. Indeed, the direct LBM calculation is the only numerical approach taking into account all installation effects on the radiated noise. In addition to these raw spectra analyses, a spectrum correction similar to the one proposed to account for turbulence grid variability on the turbulence spectra is applied. Such a calibration relies on Amiet's theory which supposes that the acoustic response of an airfoil to a HIT inflow is proportional to the impinging turbulent velocity spectrum, which can be written as (here, $U^{\mathrm{exp}} = U^{\mathrm{LBM}}$ holds, since the experimental acoustic spectra have been also obtained at the same regime of

M=0.34 than in LBM.):

$$\mathrm{SPL}^{\mathrm{LBM,\ corr}}(f) = \mathrm{SPL}^{\mathrm{LBM}}(f) + 10\log\left(\frac{\varphi_{\xi\xi}^{1\mathrm{D}}(f, U^{\mathrm{exp}}, \mathrm{TI}^{\mathrm{exp}}, {L_l}^{\mathrm{exp}})}{\varphi_{\xi\xi}^{1\mathrm{D}}(f, U^{\mathrm{LBM}}, \mathrm{TI}^{\mathrm{LBM}}, {L_l}^{\mathrm{LBM}})}\right) \quad (6)$$

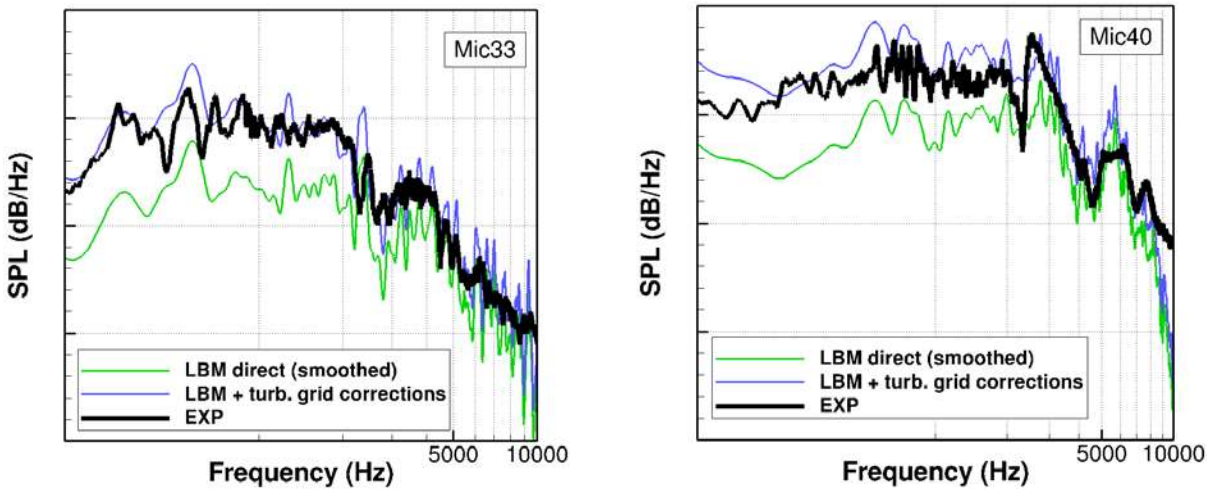

Figure 21. SPL comparisons on baseline case: direct LBM results (with and without correction) vs. experiment at Mach 0.34 for mic. 33 (left) and mic 40 (right) ; Log x-scale and 10 dB step between major y-ticks.

The validity of this simple correction is demonstrated in Figure 21 by comparing the raw (in green) and corrected (in blue) LBM solutions with experiment, using a logarithmic frequency scale. A significant level deviation with the raw solution is clearly observed, whereas the corrected LBM spectra are matching fairly well with the measurements. Moreover, complementary results provided Appendix A after the test campaign with the up-to-date grid show similar trends, demonstrating again the relevance of this 1D correction. As illustrated by the OASPL directivities (taking into account the 1D calibration) of the acoustic field plotted in Figure 22, a good agreement is observed particularly for the quadrant with negative observation angles. However, only with the LBM direct solution the shape is well captured in comparison with the experimental directivity for the upper quadrant (positive angles) contrary to LBM indirect solution. Indeed, the scattering on the sides plates is not captured with the analogy, plate surfaces of the test section not being

accounted for. Moreover, LBM direct approach is to capture the level increase observed at angles closest to the axis and attributed to vortical flow contributions.

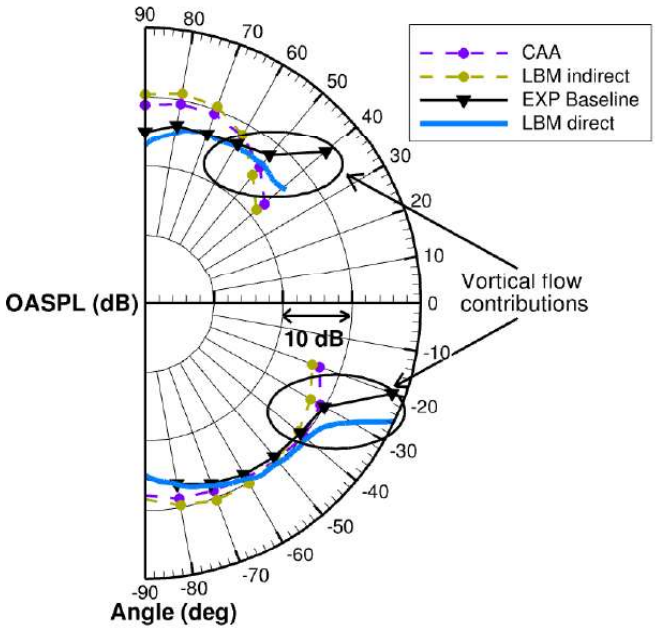

Figure 22 : OASPL (from 100 Hz to 10 kHz) noise levels from CAA, LBM, and experimental data.

4.2 Noise reduction assessment

In order to estimate the noise reduction in terms of sound power, noted $\Delta\mathrm{PWL}$, the SPL spectra are integrated over the microphone array using a basic expression as used in [2]:

$$\Delta\,\mathrm{PWL}\,(\mathrm{dB}) = 10\log\left(\frac{\sum_{\mathrm{mics\ in}\ \theta}\mathrm{SPL}_{\mathrm{baseline}}(\theta)}{\sum_{\mathrm{mics\ in}\ \theta}\mathrm{SPL}_{\mathrm{serrated}}(\theta)}\right) \quad (7)$$

Then the $\Delta\mathrm{PWL}$ spectrum from predictions and measurements is obtained by subtracting the serration-based spectrum to the baseline one.

A semi-empirical log law proposed by Paruchuri [2] is also considered to get a raw estimation of $\Delta\mathrm{PWL}$ based on a suited Strouhal number (S_t), which writes:

$$\Delta\,\mathrm{PWL}\,(\mathrm{dB}) = 10\log\left(St = f\frac{h_s}{U}\right) + 10 \quad (8)$$

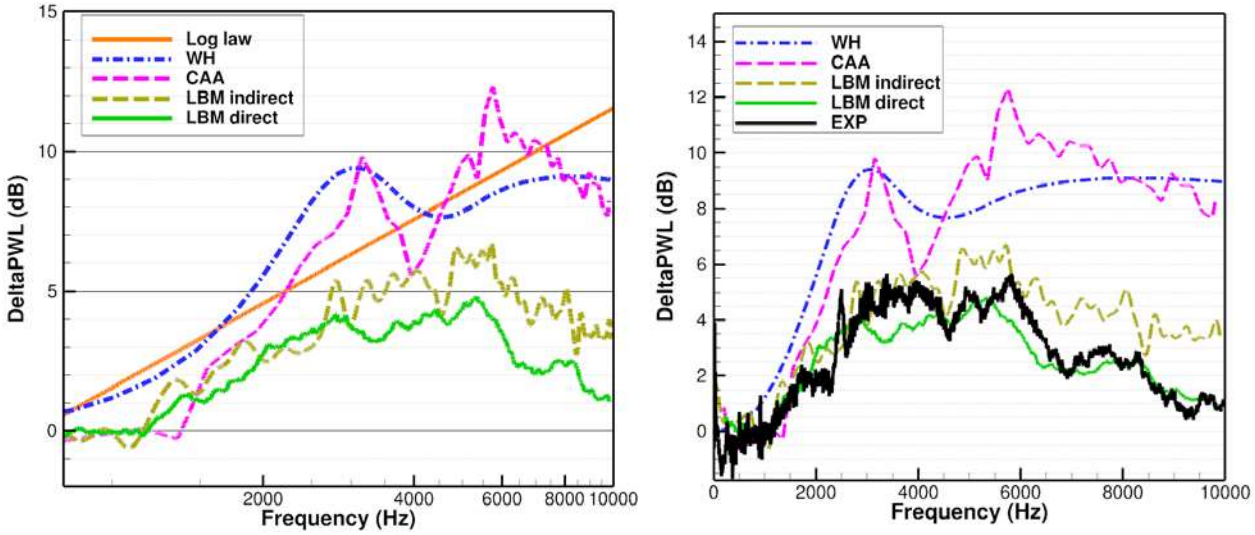

Figure 23. $\Delta\mathrm{PWL}$ assessment for design d_1 (M = 0.34). Predictions and Log law with Log x-scale (left) — Predictions Vs. experiment with linear x-scale (right).

First of all, a close trend is observed between the analytical solution (Wiener-Hopf) and the CAA with synthetic turbulence in Figure 23, which is consistent with the fact that both methods model the same underlying physics except for the geometry of the vanes. Contrary to these approaches, the LBM does not solely simulate the leading edge noise attributed to turbulence-airfoil interaction mechanism, but is expected to capture additional sources, such as trailing edge noise and scattering effects due to the presence of side plates, which probably explains the difference in the achieved noise reduction (around 4 dB less). As already noticed for the SPL predictions on the baseline case (Figure 21), the $\Delta\mathrm{PWL}$ from the LBM solutions is close to the experiments, especially for the direct solution. However, the sensitivity to the installations effect appears to be small on the noise reduction, since the FWH post-treatment provides rather close trends. Indeed, the installation effects are both taken into account for baseline and serrated geometries. Thus, it is interesting to look more closely at differences between the CAA+FWH and LBM+FWH approaches. In order to try to isolate the turbulence-airfoil interaction sources, the considered surfacic integration in the FWH post-processing is limited to the leading edge region of the vanes as illustrated in Figure 24, (left), for both the baseline and lownoise geometries. Moreover, top and bottom sides are discarded to avoid taking into account the corner flow separation.

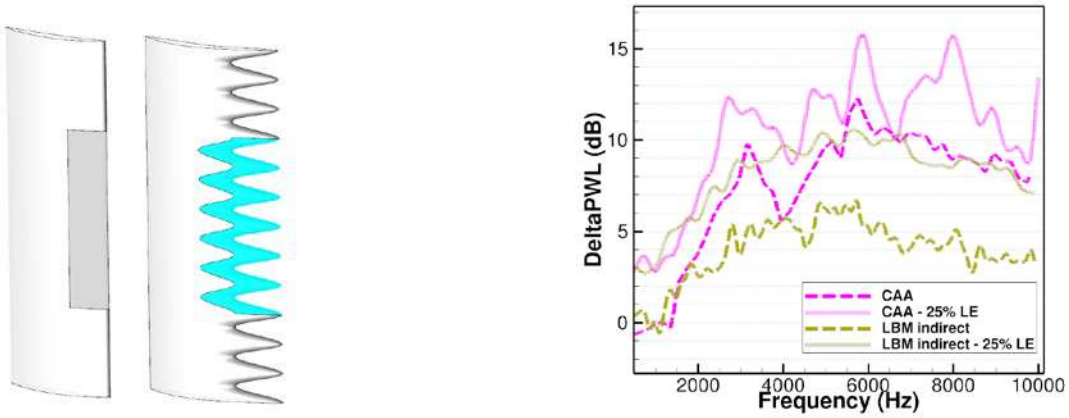

Figure 24 Sketch showing the considered FWH integration surface limited to 25 % of the chord and discarding top and bottom sides (left). Noise reductions obtained with FWH from CAA or LBM data (right).

Moreover, to avoid side effects, the integration is focused around the mid-span region, as illustrated in Figure 24 (left). Noise reduction spectra achieved with these restrictions are compared to the previous solution from Figure 23 obtained with a full integration over the skin. Deviations between LBM-based and CAA-based predictions with restricted integration are greatly reduced, which might be due to the removal of extra sources around the mid-chord (visible in LBM solutions in Figure 18). However, some discrepancies still remain which the authors expect to be attributed to the turbulence characteristics impinging the vanes: (1) HIT in the CAA and (2) anisotropic/inhomogeneous turbulence in LBM.

Finally, the noise reduction are also compared between d_1 and d_2 designs for both LBM simulations and experimental data at the M = 0.34 operating point in Figure 25. Since the chord in assumed to be infinite in the Wiener-Hopf model with flat plate assumption, the acoustic performance differences between designs d_1 and d_2 could not be assessed.

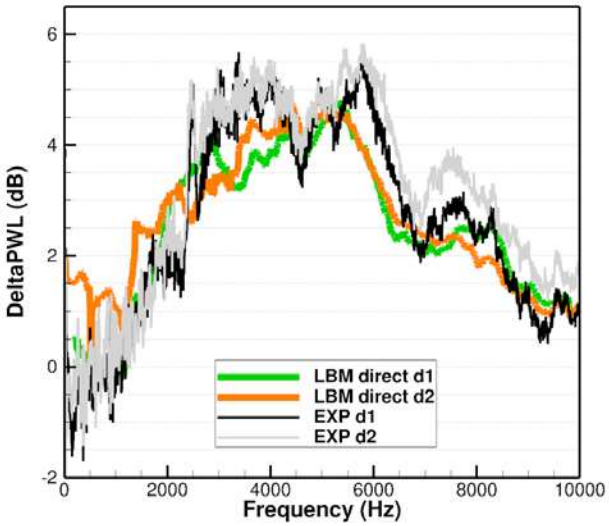

Figure 25. Noise reduction assessment at the approach condition (M = 0.34) for d_1 and d_2 designs.

The noise reductions presented in Figure 25 are almost identical for both designs and even slightly increased with the design d_2, which is aerodynamically optimized. This slight benefit may be due to less intense vortices generated at the serration roots as well as possible local flow detachments resulting in additional sources [32][33]. One may ask why the noise reduction is similar between simulations and experimental data although the turbulence length scale observed during the test campaign ($L_l \approx 12.6$ mm) does not match exactly the value adopted for the serration design criterion $\lambda_s = 2L_l$ (with $L_l = 8\,\mathrm{mm}$). A fair answer is that the sensitivity around this theoretical-based and partly empirical-based optimum value of λ_s with regards to L_l is rather low (compared to the sensitivity with respect to the h_s value) as shown experimentally in [31] for example, which might explain why differences observed in Figure 25 are not more significant.

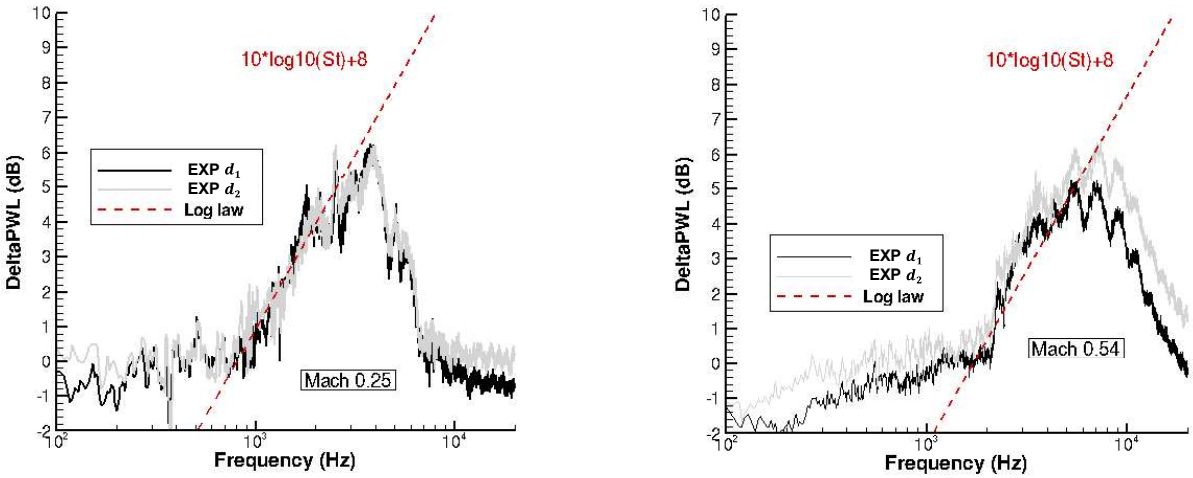

Figure 26. ΔPWL measured for d_1 and d_2 designs Mach 0.25 (left) and Mach 0.54 (right).

In addition, noise reduction for both designs d_1 and d_2 issued from experimental campaign have been assessed at two other inflow regimes: M = 0.25 and M = 0.54, as illustrated in Figure 26. Acoustic performances are similar at these velocity regimes with a frequency of the peak of noise reduction increasing almost linearly with the inflow velocity, as shown by the log law already discussed and relying on the Strouhal. The constant from the log law (set equal to 10 by Paruchuri [31]) has been modified here to better fit the present experimental results: PWL (dB) = 10 log(St) + 8. A similar modification with another constant was also suggested in [15]. This practical semi-empirical law (with appropriate tuning from isolated airfoil to cascade vanes) is found again to provide a satisfactory $\Delta\mathrm{PWL}$ estimator for pre-design purposes.

5. Conclusion

Looking at future quiet turbofans, a low-noise treatment based on leading edge serrations applied to a rectilinear cascade configuration has been numerically and experimentally investigated in this study. The efficiency on acoustic performances of the serration designs proposed by ONERA have been evaluated using a semi-analytical model based on a Wiener-Hopf formulation, and also from CAA simulations based on linearized Euler equations combined with synthetic turbulence fields [10]. In the present

work, these predictions have been complemented by high-fidelity LBM calculations, and compared with measurements achieved in the subsonic anechoic wind tunnel at LMFA.

The LBM set-up enables the modeling of the full experimental test bench, as well as a realistic description of turbulence noise sources and direct aeroacoustic predictions up to far-field microphone locations. These numerical simulations were performed before the experimental test campaign using a priori parameters, leading to a mismatch for the size of the turbulence grid. To mitigate this issue, a simple theoretical one-dimensional correction has been proposed and applied to the turbulence spectra computed from LBM simulations with success. This correction appears useful to easily consider a modification of the turbulence grid size in other contexts.

In addition, a very good agreement has been observed between RANS, LBM, and experiments on the pressure coefficient and between LBM and experiments on the far-field acoustics both in terms of noise directivity and noise reduction from serrations. Comparing those methods with different fidelity levels on a dedicated cascade test case also allowed a better understanding of the limitations from the assumptions of the respective approaches. For instance, the analytical and CAA solutions are comparing fairly well as they are both solely devoted to the leading-edge noise modeling, but then tend to overpredict the noise reduction in the actual cascade rig configuration where inherent additional noise sources or installation effects are at play. Moreover, all acoustic solutions used a FWH extrapolation for the far-field forecasting apart from the LBM with a direct approach, which has shown the closest agreement to the experimental data both in terms of pressure PSD and sound power reduction spectra. Indeed, the LBM can reproduce a more realistic turbulence field while accounting for secondary noise sources and installation effects.

All these comparisons also enabled to validate the design methodology for blades with serrations previously set up [10], both with respect to acoustic and aerodynamic behavior. In particular, it has been demonstrated that the sinusoidal leading-edge designs proposed

by ONERA can significantly reduce the broadband noise up to 5 dB in an installed configuration, while remaining robust to slight changes of the turbulent properties around the optimal value. It has also been shown that the semi-empirical law with an appropriate tuning from isolated airfoil to cascade vanes, is able to provide a satisfactory $\Delta\mathrm{PWL}$ estimator for pre-design purposes on simplified configurations.

Appendix

A) LBM simulations obtained with the up-to-date grid geometry

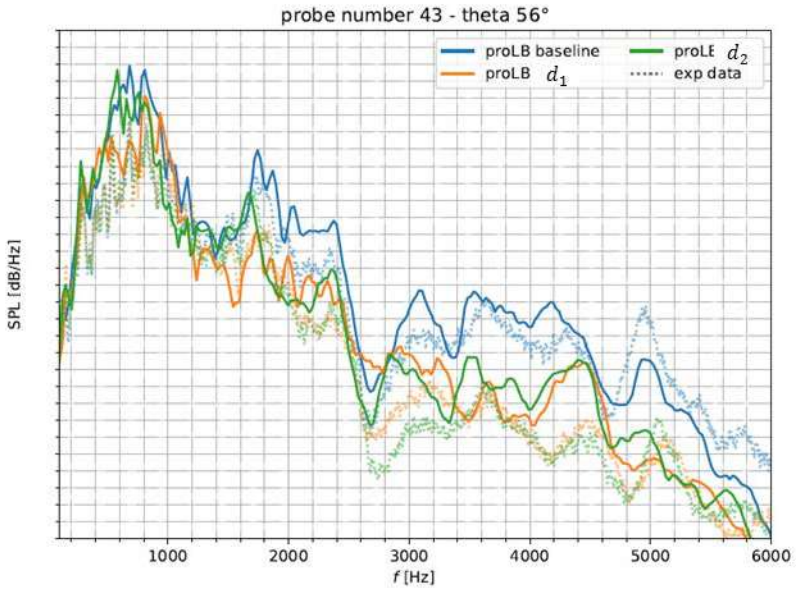

Figure A.1. SPL spectra from LBM simulation performed at CERFACS, 1 dB step between y-ticks

Figure A.1 shows results obtained by Vienne [37] from LBM simulation. The correct dimensions of the turbulence used during the test campaign have been considered, demonstrating again the relevance of the direct approach for far-field acoustic predictions. These solutions support the analytical correction proposed in this study using Eq. (5). Moreover, these results obtained independently of this work confirm the significant SPL reduction from designs d_1 and d_2 (ON1 and ON2 in the caption); with similar efficiencies than those discussed in Section 4.2.

Copyright Statement

Acknowledgements

The authors would like to thank Safran Aircraft Engines for contributing to the technical requirements of the experimental test campaign. This collaborative work between Ecole Centrale de Lyon and ONERA has received respective funding from the Clean Sky 2 Joint Undertaking (JU) under the European Union's Horizon 2020 research and innovation program under grant agreement n°865007 (InnoSTAT project), and from European Union's Horizon 2020 research and innovation program in the frame of ADEC project of CS2 LPA-IADP. This publication reflects only the author's view and the JU is not responsible for any use that may be of the information it contains.

Moreover, the authors would like to thank Lucien Vienne for sharing numerical results reported in Appendix A.

Finally, the authors would like to thank Raluca Maier (COMOTI) for the OGV manufacturing and Pascal Souchotte and Emmanuel Jondeau (Laboratoire de Mécanique des Fluides et d'Acoustique) who took part in the experimental campaign.

References

[1] D. Casalino, F. Diozzi, R. Sannino, A. Paonessa, Aircraft noise reduction technologies: A bibliographic review, Aerospace Science and Technology, Volume 12, Issue 1, 2008, Pages 1-17, ISSN 1270-9638, https://doi.org/10.1016/j.ast.2007.10.004

[2] P. Chaitanya, P. Joseph, S. Narayanan, C. Vanderwel, J. Turner, J. W. Kim, and B. Ganapathisubramani. Performance and mechanism of sinusoidal leading edge

serrations for the reduction of turbulence–aerofoil interaction noise. Journal of Fluid Mechanics, 818:435–464, 2017. doi:10.1017/jfm.2017.141.

[3] L. Ayton and C. Paruchuri. An analytical and experimental investigation of aerofoil–turbulence interaction noise for plates with spanwise-varying leading edges. Journal of Fluid Mechanics, 865:137–168, 2019. doi: 10.1017/jfm.2019.78.

[4] V. Clair, C. Polacsek, T. L. Garrec, G. Reboul, M. Gruber, and P. Joseph. Experimental and numerical investigation of turbulence-airfoil noise reduction using wavy edges. AIAA Journal, 51:2695–2713, 11 2013. doi: 10.2514/1.J052394.

[5] C. Teruna, F. Avallone, D. Casalino, and D. Ragni. Numerical investigation of leading edge noise reduction on a rod-airfoil configuration using porous materials and serrations. Journal of Sound, and Vibration, 494:115880, 2021. ISSN 0022-460X. doi: https://doi.org/10.1016/j.jsv.2020.115880.

[6] C. Polacsek, A. Cader, M. Buszyk, R. Barrier, F. Gea-Aguilera, and H. Posson. Aeroacoustic design and broadband noise predictions of a fan stage with serrated outlet guide vanes. Physics of fluids, 32(10):107107, 2020.

[7] C. Teruna, L. F. Rego, D. Casalino, D. Ragni, and F. Avallone. Full-Scale Application of Porous Leading-Edge Treatments in a Fan Stage for Mitigating Rotor-Stator Interaction Noise. 2022. doi:10.2514/6.2022-2963. URL https://arc.aiaa.org/doi/abs/10.2514/6.2022-2963.

[8] D. Casalino, F. Avallone, I. Gonzalez-Martino, and D. Ragni. Aeroacoustic study of a wavy stator leading edge in a realistic fan/OGV stage. Journal of Sound and Vibration, 442:138–154, 2019. ISSN 0022-460X. doi: https://doi.org/10.1016/j.jsv.2018.10.057.

[9] L. Mazella, C. C. Paruchuri, G. Lacagnina, Y. Mao, and P. Joseph. Experimental investigation of the noise control performance of leading edge serrations in a rectilinear cascade. 2019. doi:10.2514/6.2019-2472.

[10] M. Buszyk, C. Polacsek, T. Le Garrec, R. Barrier, and C. Bailly. Numerical Assessment of Turbulence-Cascade Noise Reduction and Aerodynamic Penalties from Serrations. AIAA Journal 2022 60:6, 3603-3619.

[11] M. Buszyk, T. Le Garrec, C. Polacsek, R. Barrier. Lattice Boltzmann simulations in a rectilinear cascade configuration for the turbulence-airfoil interaction noise evaluation and reduction through serrated leading edges. EURONOISE 2021, Oct 2021, Virtuel, Portugal. ⟨hal-03396128⟩

[12] C. Polacsek, M. Buszyk, R. Barrier, V. Clair, E. Salze. Aeroacoustic performances of a low-noise airfoil cascade with serrated leading edges: predictions and measurements. ICAS 2022, Sep 2022, STOCKHOLM, Sweden. ⟨hal-03938107⟩

[13] M. Buszyk, L. Vienne, T. Le Garrec, J-F. Boussuge, C. Polacsek, Raphaël Barrier, Vincent Clair, Edouard Salze. Lattice Boltzmann method for broadband noise predictions on a turbulence-cascade test rig including serrated vanes. ICAS 2022, Sep 2022, STOCKHOLM, Sweden.

[14] A. Finez, M. Jacob, M. Roger, and E. Jondeau. Broadband Noise Reduction Of Linear Cascades With Trailing Edge Serrations. 2011. doi: 10.2514/6.2011-2874. URL https://arc.aiaa.org/doi/abs/10.2514/6.2011-2874.

[15] G. Bampanis, M. Roger, D. Ragni, F. Avallone, and C. Teruna. Airfoil-turbulence interaction noise source identification and its reduction by means of leading edge serrations. In 25th AIAA/CEAS Aeroacoustics Conference, 2019. doi: 10.2514/6.2019-2741. URL https://arc.aiaa.org/doi/abs/10.2514/6.2019-2741.

[16] T. M. Biedermann, P. Czeckay, T. F. Geyer, F. Kameier, and C. O. Paschereit. Effect of inflow conditions on the noise reduction through leading edge serrations. AIAA Journal, 57(9):4104–4109, 2019. doi: 10.2514/1.J057831.

[17] S. Redonnet. Simulation de la propagation acoustique en présence

d'écoulements quelconques et de structures solides par résolution numérique des équations d'Euler. PhD thesis, Université de Bordeaux, 2001. URL https://books.google.fr/books?id=IBPgzQEACAAJ.

[18] V. Clair. Calcul numérique de la réponse acoustique d'un aubage soumis à un sillage turbulent. PhD thesis, Université Claude Bernard - Lyon I, Nov. 2013.

[19] C. K. W. Tam and Z. Dong. Radiation and outflow boundary conditions for direct computation of acoustic and flow disturbances in a nonuniform mean flow. Journal of Computational Acoustics, 04(02):175–201, 1996. doi: 10.1142/S0218396X96000040.

[20] J. E. Ffowcs Williams, D. L. Hawkings, and M. J. Lighthill. Sound generation by turbulence and surfaces in arbitrary motion. Philosophical Transactions of the Royal Society of London. Series A, Mathematical and Physical Sciences, 264(1151):321–342, 1969. doi: 10.1098/rsta.1969.0031.

[21] G. Reboul. Modélisation du bruit à large bande de soufflantes de turboréacteurs. Theses, Ecole Centrale de Lyon, Nov. 2010. URL https://tel.archives-ouvertes.fr/tel-00562647.

[22] URL http://www.prolb-cfd.com/

[23] X. Shan, X.-F. Yuan, and H. Chen. Kinetic theory representation of hydrodynamics: a way beyond the navier–stokes equation. Journal of Fluid Mechanics, 550:413–441, 2006. doi: 10.1017/S0022112005008153.

[24] J. Jacob, O. Malaspinas, and P. Sagaut. A new hybrid recursive regularised Bhatnagar–Gross–Krook collision model for lattice Boltzmann method-based large eddy simulation. Journal of Turbulence, pages 1 – 26, Nov. 2018. doi: 10.1080/14685248.2018.1540879. URL https://hal.archives-ouvertes.fr/hal-02114308.

[25] T. Astoul. Towards improved lattice Boltzmann aeroacoustic simulations with

non-uniform grids: application to landing gears noise prediction. PhD thesis, Aix-Marseille Université, 2021.

[26] Y. Feng, P. Boivin, J. Jacob, and P. Sagaut. Hybrid recursive regularized thermal lattice Boltzmann model for high subsonic compressible flows. Journal of Computational Physics, 394:82–99, 2019. ISSN 0021-9991. doi: https://doi.org/10.1016/j.jcp.2019.05.031.

[27] S. Guo, Y. Feng, J. Jacob, F. Renard, and P. Sagaut. An efficient lattice Boltzmann method for compressible aerodynamics on d3q19 lattice. Journal of Computational Physics, 418:109570, 2020. ISSN0021-9991. doi: https://doi.org/10.1016/j.jcp.2020.109570.

[28] T. Astoul, G. Wissocq, J.-F. Boussuge, A. Sengissen, and P. Sagaut. Lattice Boltzmann method for computational aeroacoustics on non-uniform meshes: A direct grid coupling approach. Journal of Computational Physics, 447:110667, Dec. 2021. doi: 10.1016/j.jcp.2021.110667.

[29] E. Lévêque, F. Toschi, L. Shao, and J.-P. Bertoglio. Shear-improved Smagorinsky model for large-eddy simulation of wall-bounded turbulent flows. Journal of Fluid Mechanics, 570:491–502, 2007. doi: 10.1017/S0022112006003429.

[30] F. G. Aguilera, J. R. Gill, D. Angland, and X. Zhang. Wavy Leading Edge Airfoils Interacting with Anisotropic Turbulence. 2017. doi: 10.2514/6.2017-3370.

[31] C. Paruchuri. Aerofoil geometry effects on turbulence interaction noise. PhD thesis, University of Southampton, April 2017.

[32] D. Lewis, S. Moreau, M. C. Jacob, and M. Sanjosé. ACAT1 Fan Stage Broadband Noise Prediction Using Large-Eddy Simulation and Analytical Models. AIAA Journal 2022 60:1, 360-380.

[33] B. François, C. Polacsek, and R. Barrier. Zonal Detached Eddy Simulation of

the Fan-Outlet Guide, Vanes Stage of a Turbofan Engine: Part I—Methodology, Numerical Setup, and Aerodynamic Analysis. Journal of Turbomachinery, 144(11), 07 2022. ISSN 0889-504X. doi: 10.1115/1.4054528. 111004.

[34] M. Buszyk. Aeroacoustics of leading edge serrations for turbulence-cascade interaction noise reduction. PhD thesis, Ecole Centrale de Lyon, 2022ECDL0023, 2022.

[35] P. Sagaut, and C. Cambon. (2008). Homogeneous Turbulence Dynamics. 10.1017/CBO9780511546099.

[36] https://cordis.europa.eu/project/id/865007

[37] L. Vienne, 2022, CERFACS, private communication.

[38] N. Afzal. Wake layer in a thermal turbulent boundary layer with pressure gradient. International Journal of Heat and Mass Transfer, 1999. 10, 39, 88, 147, 165.

[39] S. Wilhelm, J. Jacob, and P. Sagaut. An explicit power-law-based wall model for lattice Boltzmann method-Reynolds-averaged numerical simulations of the flow around airfoils. Physics of Fluids, 30, 2018. 9, 10, 11, 39, 147.